Effect of evanescent modes and chaos on deterministic scattering in electron waveguides

G. Akguc and L. E. Reichl

Center for Studies in Statistical Mechanics and Complex Systems, University of Texas at Austin, Austin, Texas 78712
(Received 22 November 2000; revised manuscript received 29 June 2001; published 24 October 2001)

Statistical properties of Wigner delay times and the effect of evanescent modes on the deterministic scattering of an electron matter wave from a classically chaotic two-dimensional electron waveguide are studied for the case of 2, 6, and 16 propagating modes. Deterministic reaction matrix theory for this system is generalized to include the effect of evanescent modes on the scattering process. The statistical properties of the Wigner delay times for the deterministic scattering process are compared to the predictions of random reaction matrix theory.

I. INTRODUCTION

In the 1950s it was observed that nuclear scattering processes can have statistical properties indistinguishable from random scattering processes [1]. The first hint that these random elements in the nuclear scattering data might be due to underlying chaos in the nuclear dynamics, appeared in a paper by McDonald and Kauffman [2], who studied the energy level statistics for closed quantum billiards whose classical counterparts are either integrable or chaotic. They found that the quantized energy levels of the chaotic billiard had a statistical distribution that matched predictions of random matrix theory. The first studies of the scattering properties of completely chaotic quantum systems with few degrees of freedom were due to Smilansky and co-workers [3], and since then a number of papers have appeared [4,5] analyzing quantum scattering using semiclassical techniques [6–8], and focused on the semiclassical regime. Recently we [9] studied deterministic quantum scattering from a chaotic billiard, in a regime where only a few channels are open, using finite element techniques and found random signatures in the Wigner delay times.

The analysis of fully quantum-mechanical scattering processes, in systems where only a few channels are open, is not easily accessible because this regime is numerically demanding. This fact has led to renewed interest in the reaction matrix formulation of scattering theory that was developed by Wigner and Eisenbud [10] in the late 1940s [11]. The idea behind reaction matrix theory is to decompose configuration space into a reaction region (cavity) and an asymptotic scattering region (lead). The exact wave function in the reaction region can be expanded in terms of any convenient complete set of states with fixed boundary conditions on the surface of the reaction region, provided the coupling between the reaction region (cavity) and asymptotic scattering region is singular [12,13].

Reaction matrix theory provides a convenient framework for predicting the scattering properties of systems governed by random Hamiltonian matrices. We shall call the theory that uses reaction matrices to predict the scattering properties of systems with Gaussian random Hamiltonians, *random reaction matrix theory* (RRMT). The predictions of RRMT have been compared to experimental nuclear scattering data [14], scattering in electron waveguides [15], and resonances in acoustic and microwave resonators [16], under conditions in which these systems are thought to have classically chaotic dynamics. These predictions, in turn, can be compared to the scattering properties of chaotic systems. RRMT, as it is currently formulated, neglects some possibly important effects in the scattering process, namely, the effect of evanescent modes and some of the energy dependence of resonance poles.

In this paper, we will study the deterministic scattering of an electron in a two-dimensional electron waveguide, which has a classically chaotic cavity formed by a ripple billiard connected to a lead at one end (see Fig. 1). We will compare the results of deterministic scattering from the chaotic cavity to the predictions of random matrix theory. The ripple billiard is particularly well suited to the use of reaction matrix theory, because a simple coordinate transformation allows us to construct a Hamiltonian matrix and thus an eigenvalue equation for the basis states inside the cavity. This has not been done for any other form of chaotic billiard that we know of.

We will generalize the reaction matrix theory for two-dimensional waveguides to include the effect of evanescent modes explicitly and exactly in our expression for the S matrix. (The effect of evanescent modes on scattering processes
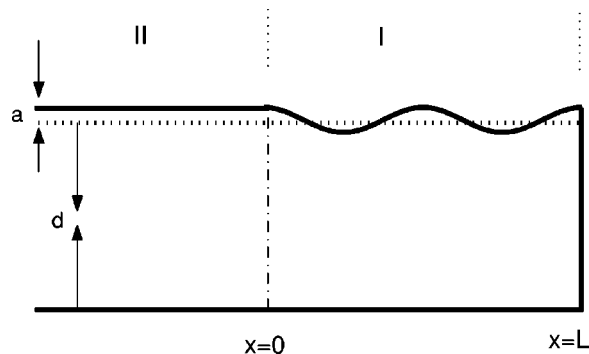
FIG. 1. Geometry of the two-dimensional electron waveguide used in our calculations. The rippled waveguide is the region defined by solid lines, rectangular waveguide is the region whose upper boundary is given by the dotted line. The dotted-dashed line shows the interference between leads and scattering region. Here ''a'' is the width of the ripple, ''ds'' is the width of the rectangular waveguide, scattering cavity extends from $x=0$ to $x=L$

has been studied for nuclear scattering processes [17–20] using approximate theories.) We will show that for the waveguide we consider, evanescent modes dominate the scattering properties of the waveguide in energy regions where new propagating channels open.

We begin, in Sec. II, by developing the reaction matrix theory of deterministic scattering in our electron waveguide, starting from a configuration space formulation rather than the usual eigenmode formulation, and we construct the Hamiltonians for the cavity (reaction region) and leads (asymptotic scattering region) of an electron waveguide. In Sec. III, we derive the reaction matrix. In Sec. IV, we derive the scattering matrix. In Sec. V, we describe the method we use to obtain a complete set of basis states for a cavity with a rippled wall. In Sec. VI, we discuss the effect of evanescent modes on the scattering process, and in Sec. VII we compare the statistical properties of the Wigner delay times for deterministic scattering in the waveguide with predictions of RRMT. Finally, in Sec. VIII, we make some concluding remarks.

II. SCATTERING HAMILTONIAN

We will consider the scattering properties of an electron with mass m in the waveguide shown in Fig. 1. The electron enters from the left with energy E along an infinitely long straight lead that has infinitely hard walls. The electron wave is reflected back to the left by an infinitely hard wall located at $x=L$. The scattering is strongly affected by the region $0 < x < L$ (the cavity) in which the upper wall is rippled, and the dynamics inside the cavity can be chaotic.

The Schroedinger equation, which describes propagation of a particle wave, $\Psi(x,y,t)$, for all times t is given by

$$i\hbar \frac{\partial \Psi(x,y,t)}{\partial t} = \left[-\frac{\hbar^2}{2m}\left(\frac{\partial^2}{\partial x^2} + \frac{\partial^2}{\partial y^2} \right) + V(x,y) \right] \Psi(x,y,t), \tag{1}$$

where $\hbar$ is Planck's constant. The potential $V(x,y)$ has the following properties: $V(x,y)=\infty$ for $(L \leq x < \infty)$; $V(x,0) = \infty$ for $(-\infty \leq x \leq L)$; $V[x,y=g(x)]=\infty$ for $(0<x<L)$; and $V(x,y=a+d)=\infty$ for $(-\infty < x < 0)$; where $g(x)=d + a \cos(4\pi x/L)$ gives the contour of the ripple, d is the average width of the cavity, L is the length, and a is the ripple amplitude. Throughout this paper, we take the electron mass to be the effective mass of an electron in GaAs, $m = 0.067m_e$, where m_e is the free electron mass.

We can introduce projection operators,

$$\hat{P} = \int_{-\infty}^{0} dx \int_{-\infty}^{\infty} dy \quad |x,y\rangle\langle x,y|$$

and

$$\hat{Q} = \int_{0}^{\infty} dx \int_{-\infty}^{\infty} dy \quad |x,y\rangle\langle x,y|$$

that satisfy the completeness relation $\hat{Q}+\hat{P}=\hat{1}$, and separate the cavity region from the asymptotic scattering region. Here $|x,y\rangle$ is the simultaneous eigenstate of position operators $\hat{x}$

and $\hat{y}$. The projection operators $\hat{Q}$ and $\hat{P}$ have the property that $\hat{Q}=\hat{Q}^2$, $\hat{P}=\hat{P}^2$, and $\hat{Q}\hat{P}=\hat{P}\hat{Q}=0$.

The total Hamiltonian can be written

$$\hat{H}=\hat{H}_{QQ}+\hat{H}_{PP}+\hat{H}_{QP}+\hat{H}_{PQ}. \tag{2}$$

The Hamiltonian $\hat{H}_{QQ}$ in the cavity (region I in Fig. 1), can be written

$$\hat{H}_{QQ} \equiv \hat{Q}\left[\frac{1}{2m}(\hat{p}_x^2+\hat{p}_y^2) + V(\hat{x},\hat{y}) \right]\hat{Q}, \tag{3}$$

where $\hat{p}_x$ and $\hat{p}_y$ are momentum operators, m is the mass of the particle, and the potential $V(\hat{x},\hat{y})$ determines the potential walls of the cavity. The Hamiltonian $\hat{H}_{QQ}$ is Hermitian and, therefore, it will have a complete, orthonormal set of eigenstates that we denote as $\hat{Q}|\phi_j\rangle$. We can write the eigenvalue equation as $\hat{H}_{QQ}\hat{Q}|\phi_j\rangle = \lambda_j \hat{Q}|\phi_j\rangle$, where λ_j is the jth energy eigenvalue of $\hat{H}_{QQ}$ and $j=1,2,\ldots M$ (we will later let $M \to \infty$). The eigenstates $\phi_j(x,y) \equiv \langle x,y|\hat{Q}|\phi_j\rangle$ must be zero at the walls of the cavity (which are assumed infinitely hard). We will require that the eigenstates, $\phi_j(x,y)$, have zero slope at $x=0$ so that $d\phi_j/dx|_{x=0}=0$. Singular coupling, between the cavity and the lead, will correct for the fact that the actual wave function does not have zero slope at $x=0$. The completeness of the states $\hat{Q}|\phi_j\rangle$ allows us to write the completeness relation, $\Sigma_j \hat{Q}|\phi_j\rangle\langle\phi_j|\hat{Q}=\hat{Q}$. Orthonormality requires that $\langle\phi_j|\hat{Q}|\phi_{j'}\rangle = \delta_{j,j'}$.

The Hamiltonian $\hat{H}_{PP}$ in the asymptotic scattering region (region II in Fig. 1) is given by

$$\hat{H}_{PP} \equiv \hat{P}\left[\frac{1}{2m}(\hat{p}_x^2+\hat{p}_y^2) + V(\hat{x},\hat{y}) \right]\hat{P}, \tag{4}$$

where $V(\hat{x},\hat{y})$ locates the infinitely hard walls of the lead. Because the leads are assumed to be straight, the transverse parts of the energy eigenstates, in the leads, decouple from the longitudinal part. The eigenstates of $\hat{H}_{PP}$ are denoted $\hat{P}|\Phi_{k_n,n}\rangle$ and satisfy the eigenvalue equation

$$\hat{H}_{PP}\hat{P}|\Phi_{k_n,n}\rangle = E_{k_n,n}\hat{P}|\Phi_{k_n,n}\rangle = \frac{\hbar^2}{2m}\left[k_n^2 + \left(\frac{n\pi}{w}\right)^2 \right]\hat{P}|\Phi_{k_n,n}\rangle, \tag{5}$$

where w is the width of the lead. The eigenstate $\hat{P}|\Phi_{k_n,n}\rangle$ in configuration space can be written

$$\langle x,y|\hat{P}|\Phi_{k_n,n}\rangle = \chi_{k,n}(x)\sqrt{\frac{2}{w}}\sin\left(\frac{n\pi y}{w}\right) \tag{6}$$

The state $\hat{P}|\Phi_{k_n,n}\rangle$ is called the nth channel state.

The coupling between the cavity and the lead is given by

$$\hat{H}_{QP}=C\hat{Q}\,\delta(\hat{x})\hat{p}_x\hat{P} \quad \text{and} \quad \hat{H}_{PQ}=C\hat{P}\,\delta(\hat{x})\hat{p}_x\hat{Q}, \tag{7}$$

where $\langle x|\hat{p}_x|x'\rangle = \hbar/i\,\delta(x-x')d/dx$.

The waveguide energy eigenstates $|E\rangle$ satisfy the eigenvalue equation $\hat{H}|E\rangle = E|E\rangle$. The states $|E\rangle$ can be decomposed into their contributions from the two regions of configuration space, so that

$$|E\rangle = \sum_{j=1}^{M} \gamma_j \hat{Q}|\phi_j\rangle + \sum_{n=0}^{N} \Gamma_n \hat{P}|\Phi_n\rangle, \qquad (8)$$

where $\gamma_j = \langle \phi_j|\hat{Q}|E\rangle$ and $\Gamma_n = \langle \Phi_n|\hat{P}|E\rangle$. The eigenvalue equation, $\hat{H}|E\rangle = E|E\rangle$, yields a series of equations

$$\hat{H}_{QQ}\hat{Q}|\phi_j\rangle \gamma_j + \sum_{n=0}^{N} \hat{H}_{QP}\hat{P}|\Phi_n\rangle \Gamma_n = E\hat{Q}|\phi_j\rangle \gamma_j, \qquad (9)$$

for $j = 1,2,\ldots,M$ and

$$\hat{H}_{PP}\hat{P}|\Phi_n\rangle \Gamma_n + \sum_{j} H_{PQ}\hat{Q}|\phi_j\rangle \gamma_j = E\hat{P}|\Phi_n\rangle \Gamma_n \qquad (10)$$

for $n = 1,2,\ldots,N$. The condition for Hermiticity of the Hamiltonian, $\langle \Psi_\beta|\hat{H}|\Psi_\alpha\rangle = \langle \Psi_\alpha|\hat{H}|\Psi_\beta\rangle^*$, allows us to determine that the value of the coupling constant C is $C = 4\hbar i/2m$ (see [21]).

III. THE REACTION MATRIX

We now have enough information to derive the reaction matrix for this system. Let us first multiply Eq. (9) by $\langle \phi_j|\hat{Q}$ to obtain

$$(\lambda_j - E)\gamma_j + C\frac{\hbar}{4i}\sum_{n=1}^{N} \phi_{j,n}^*(0)\left(\frac{d\chi_n}{dx}\right)_{x=0}\Gamma_n = 0. \qquad (11)$$

using the coupling constant $C = 4\hbar i/2m$, we can rewrite Eq. (11) and obtain the following expression for γ_j,

$$\gamma_j = \frac{\hbar^2}{2m}\frac{1}{(E-\lambda_j)}\sum_{n=1}^{N} \phi_{j,n}^*(0)\left(\frac{d\chi_n}{dx}\right)_{x=0}\Gamma_n. \qquad (12)$$

The continuity of the energy eigenstates, at the interface between the cavity and the lead, yields

$$\Gamma_n\chi_n(0) = \sum_{j=1}^{M} \gamma_j\phi_{j,n}(0) = \sum_{n'=1}^{N} R_{n,n'}\left(\frac{d\chi_n}{dx}\right)_{x=0}\Gamma_{n'}. \qquad (13)$$

where

$$R_{n,n'} = \frac{\hbar^2}{2m}\sum_{j=1}^{M}\frac{\phi_{j,n'}^*(0)\phi_{j,n}(0)}{(E-\lambda_j)} \qquad (14)$$

is the (n,n')th matrix element of the reaction matrix.

We must distinguish between propagating and evanescent modes. The states in the leads, for propagating modes, can be written

$$\Gamma_n\chi_n(x) = \frac{a_n}{\sqrt{k_n}}e^{-ik_nx} + \frac{b_n}{\sqrt{k_n}}e^{ik_nx}, \qquad (15)$$

where

$$k_n = \sqrt{\frac{2mE}{\hbar^2} - \left(\frac{n\pi}{d+a}\right)^2} \qquad (16)$$

If there are ν propagating modes then $n = 1,2,\ldots,\nu$. Here we use a unit current normalization. The evanescent modes in the leads can be written

$$\Gamma_n\chi_n(x) = \frac{c_n}{\sqrt{k_n}}e^{-\kappa_n|x|}, \qquad (17)$$

where

$$\kappa_n = \sqrt{\left(\frac{n\pi}{d+a}\right)^2 - \frac{2mE}{\hbar^2}}. \qquad (18)$$

For evanescent modes the index $n = \nu+1,\nu+2,\ldots,N$, where $N \to \infty$.

IV. THE SCATTERING MATRIX

To obtain the scattering matrix, we must first separate the propagating modes from the evanescent modes. This first step is accomplished as follows. Using Eq. (15) and Eq. (17) we can write Eq. (13) in the matrix form

$$\begin{pmatrix} \bar{a}+\bar{b} \\ \bar{c} \end{pmatrix} = \begin{pmatrix} \bar{K}_p & 0 \\ 0 & \bar{K}_e \end{pmatrix}\begin{pmatrix} \bar{R}_{pp} & \bar{R}_{pe} \\ \bar{R}_{ep} & \bar{R}_{ee} \end{pmatrix}\begin{pmatrix} \bar{K}_p & 0 \\ 0 & \bar{K}_e \end{pmatrix}\begin{pmatrix} i(\bar{b}-\bar{a}) \\ \bar{c} \end{pmatrix},$$
$$(19)$$

where

$$\bar{a} = \begin{pmatrix} a_1 \\ \vdots \\ a_\nu \end{pmatrix}, \quad \bar{b} = \begin{pmatrix} b_1 \\ \vdots \\ b_\nu \end{pmatrix}, \quad \bar{c} = \begin{pmatrix} c_{\nu+1} \\ \vdots \\ c_N \end{pmatrix}, \qquad (20)$$

$$\bar{K}_p = \begin{pmatrix} \sqrt{k_1} & \cdots & 0 \\ \vdots & \ddots & \vdots \\ 0 & \cdots & \sqrt{k_\nu} \end{pmatrix},$$

$$\bar{K}_e = \begin{pmatrix} \sqrt{\kappa_1} & \cdots & 0 \\ \vdots & \ddots & \vdots \\ 0 & \cdots & \sqrt{\kappa_{N-\nu}} \end{pmatrix}$$

$$\bar{R}_{pp} = \begin{pmatrix} R_{1,1} & \cdots & R_{1,\nu} \\ \vdots & \cdots & \vdots \\ R_{\nu,1} & \cdots & R_{\nu,\nu} \end{pmatrix},$$

$$\bar{R}_{pe}=\begin{pmatrix} R_{1,\nu+1} & \cdots & R_{1,N} \\ \vdots & \cdots & \vdots \\ R_{\nu,\nu+1} & \cdots & R_{\nu,N} \end{pmatrix},$$

$$\bar{R}_{ep}=\begin{pmatrix} R_{\nu+1,1} & \cdots & R_{\nu+1,\nu} \\ \vdots & \cdots & \vdots \\ R_{N,1} & \cdots & R_{N,\nu} \end{pmatrix},$$

$$\bar{R}_{ee}=\begin{pmatrix} R_{\nu+1,\nu+1} & \cdots & R_{\nu+1,N} \\ \vdots & \cdots & \vdots \\ R_{N,\nu+1} & \cdots & R_{N,N} \end{pmatrix}.$$

If we expand out Eq. (19), we find

$$\bar{a}+\bar{b}=i\bar{K}_p\bar{R}_{pp}\bar{K}_p(\bar{b}-\bar{a})+\bar{K}_p\bar{R}_{pe}\bar{K}_e\bar{c}, \quad (21)$$

$$\bar{c}=i\bar{K}_e\bar{R}_{ep}\bar{K}_p(\bar{b}-\bar{a})+\bar{K}_e\bar{R}_{ee}\bar{K}_e\bar{c}. \quad (22)$$

From Eq. (22) we can write $\bar{c}$ as

$$\bar{c}=\frac{i}{(\bar{1}_e-\bar{K}_e\bar{R}_{ee}\bar{K}_e)}\bar{K}_e\bar{R}_{ep}\bar{K}_p(\bar{b}-\bar{a}), \quad (23)$$

where $\bar{1}_e$ is a unit matrix with the same dimensions as $\bar{R}_{ee}$. If we substitute Eq. (23) into Eq. (21), we find

$$\bar{a}+\bar{b}=i\bar{D}(\bar{b}-\bar{a}), \quad (24)$$

where the rescaled reaction matrix takes the form

$$\bar{D}=\left[\bar{K}_p\bar{R}_{pp}\bar{K}_p+\bar{K}_p\bar{R}_{pe}\bar{K}_e\frac{1}{(\bar{1}_e-\bar{K}_e\bar{R}_{ee}\bar{K}_e)}\bar{K}_e\bar{R}_{ep}\bar{K}_p\right]. \quad (25)$$

The second term on the right in Eq. (25) contains the effect of the evanescent states on the propagating modes in the waveguide. The *scattering matrix* $\bar{S}$ relates the outgoing propagating modes to the incoming propagating modes through the relation $\bar{a}=\bar{S}\bar{b}$. The scattering matrix is thus given by

$$\bar{S}=-\frac{(\bar{1}_p-i\bar{D})}{(\bar{1}_p+i\bar{D})}, \quad (26)$$

where $\bar{1}_p$ is a unit matrix with the same dimension as $\bar{R}_{pp}$.

We see from Eqs. (25) and (26) that the evanescent modes may play an important role in the scattering process. To see this effect on the resonance structure of the $\bar{S}$ matrix, we obtain a more explicit form as follows. First we define the coupling matrices

$$\bar{w}_{Np}\equiv\begin{pmatrix} \phi_{1,1} & \cdots & \phi_{1,\nu} \\ \vdots & & \vdots \\ \phi_{N,1} & \cdots & \phi_{N,\nu} \end{pmatrix}\bar{K}_p \quad \text{and}$$

$$\bar{w}_{Ne}\equiv\begin{pmatrix} \phi_{1,1} & \cdots & \phi_{1,N-\nu} \\ \vdots & & \vdots \\ \phi_{N,1} & \cdots & \phi_{N,N-\nu} \end{pmatrix}\bar{K}_e, \quad (27)$$

where p is the number of propagating modes and e is the number of evanescent modes in the lead. The matrix $\bar{D}$ can be written in terms of the coupling matrices as

$$\bar{D}=\bar{w}_{pN}^{\dagger}\frac{1}{E\bar{1}_N-\bar{H}_{in}}\bar{w}_{Np}$$

$$+\bar{w}_{pN}^{\dagger}\frac{1}{E\bar{1}_N-\bar{H}_{in}}\bar{w}_{Ne}\frac{1}{\bar{1}_e-\bar{w}_{eN}^{\dagger}\frac{1}{E\bar{1}_N-\bar{H}_{in}}\bar{w}_{Ne}}$$

$$\times\bar{w}_{eN}^{\dagger}\frac{1}{E\bar{1}_N-\bar{H}_{in}}\bar{w}_{Np} \quad (28)$$

where $\bar{H}_{in}$ is a diagonal matrix formed by the eigenvalues of the Hamiltonian H_{QQ} inside the cavity. This expression for $\bar{D}$ can then be substituted into Eq. (26) and, after some algebra, we obtain the following form for the scattering matrix,

$$\bar{S}=-\left(1-2i\bar{w}_{pN}^{\dagger}\frac{1}{E\bar{1}_N-\bar{H}_{in}-\bar{w}_{Ne}\bar{w}_{eN}^{\dagger}+i\bar{w}_{Np}\bar{w}_{pN}^{\dagger}}\bar{w}_{Np}\right). \quad (29)$$

As can be seen from the denominator of this expression, evanescent modes affect the positions of resonance poles in the complex energy plane because of the dependence of the S matrix on $\bar{w}_{eN}$.

V. BASIS STATES FOR THE CAVITY REGION

We now describe a method to obtain the complete set of eigenstates $\hat{Q}|\phi_j\rangle$ for the ripple cavity. We will require that these states have zero slope at the cavity-lead interface ($x=0$). The eigenvalue equation, $H_{QQ}\hat{Q}|\phi_j\rangle=\lambda_j\hat{Q}|\phi_j\rangle$ in configuration space, takes the form

$$\frac{-\hbar^2}{2m}\left(\frac{d^2}{dx^2}+\frac{d^2}{dy^2}+V(x,y)\right)\phi_j(x,y)=\lambda_j\phi_j(x,y), \quad (30)$$

where $\phi_j(x,y)\equiv\langle x,y|\hat{Q}|\phi_j\rangle$. After the coordinate change [9,22],

$$u=x, \quad v=\frac{y}{d+a\cos\left(\frac{4\pi}{L}x\right)}, \quad (31)$$

we obtain an eigenvalue equation in terms of the coordinates u and v given by

$$\bar{H}\psi_j(u,v) \equiv -\frac{\hbar^2}{2m}(\partial_u^2 + h_1\partial_v^2 + h_2\partial_{uv}^2 + h_3\partial_v)\psi_j(u,v)$$

$$= \lambda_j\psi_j(u,v) \qquad (32)$$

where

$$h_1 = \frac{1 + v^2 g_u^2}{g^2}, \quad h_2 = \frac{-2vg_u}{g}, \quad h_3 = \frac{-vg_{uu}}{g} + \frac{2vg_u^2}{g^2},$$

$g = g(u) \equiv d + a\cos[(4\pi/L)u]$, $g_u \equiv \partial g/\partial u$, and $\psi_j(u,v) = \phi_j(x(u,v),y(u,v))$. The boundary conditions in (u,v) space are given by $\partial_u\psi_j(0,v)=0$, $\psi_j(L,v)=0$, $\psi_j(u,0)=0$, and $\psi_j(u,1)=0$, so that in terms of these coordinates the walls are straight. Note that in the (u,v) coordinate frame, the states, $\psi_j(u,v)$ are normalized with a weighting factor $g(u)$ so that

$$\int\int g(u)\psi_j^\dagger(u,v)\psi_{j'}(u,v)du\,dv = \delta_{j,j'}, \qquad (33)$$

The state, $\psi_j(u,v)$, can be expanded in terms of a Fourier basis

$$\psi_j(u,v) = \sum_{m=1}^{\infty}\sum_{n=1}^{\infty} B_{mn}^j\phi_{mn}(u,v) \qquad (34)$$

with

$$\phi_{mn}(u,v) = \frac{2}{\sqrt{L}}g^{-1/2}\sin(n\pi v)\cos\left[\frac{(2m-1)\pi u}{2L}\right], \qquad (35)$$

where B_{mn}^j are the unknown expansion coefficients. As a result of this expansion, the boundary value problem is transformed into the eigenvalue problem

$$\sum_{m=1}^{\infty}\sum_{n=1}^{\infty} H_{mnm'n'}B_{m'n'}^j = E_jB_{mn}^j. \qquad (36)$$

The Hamiltonian matrix elements $H_{mnm'n'}$ are given by

$$H_{mnm'n'} = \frac{4}{L}\int_0^L du\int_0^1 dv\,\sqrt{g}\,\sin(n\pi v)f\,\bar{H}(\sin(n'\pi v)f'/\sqrt{g}) \qquad (37)$$

where $f \equiv \cos[(2m-1)\pi u/2L]$, $f' \equiv \cos[(2m'-1)\pi u/2L]$, $g \equiv d + a\cos[(4\pi/L)u]$, and $\bar{H}$ is the differential operator defined in Eq. (32). Note that we cannot use integration by parts to get a symmetrical form, as was done in Refs. [9] and [22] because surface terms will not drop out.

The eigenvalues and eigenvectors of $\bar{H}$ can be calculated efficiently due to the sinusoidal integrals. Eigenvectors of $\bar{H}$ give values for the expansion coefficients B_{mn}^j and the eigenfunctions in u-v space can be found from these coefficients.

The solution can then be transformed back to x-y space to obtain the basis states $\phi_j(x,y)$.

VI. THE EFFECT OF EVANESCENT MODES

For the ripple cavity considered here, the effect of evanescent modes on Wigner delay times is most important at energies just before a new channel opens in the lead. We have studied the effect of evanescent modes using parameters, $a = 10$ Å, $d = 100$ Å, $L = 500$ Å, and $m = 0.067m_e$, and we use the form of the S matrix in Eq. (26) to obtain our results. We compare the variation of S-matrix elements S_{ij} for an S matrix that includes the evanescent modes ($\bar{w}_{Ne} \neq 0$), with an S matrix $\bar{S}^0$, which excludes evanescent modes ($\bar{w}_{Ne}=0$). We use the cavity length, $L = 500$ Å to increase the density of resonances in any given energy interval. In a mesh based numerical method (like a finite element or a finite difference) increasing cavity length is numerically not efficient due to the increasing number of nodal points, but the reaction matrix approach can easily accommodate longer cavities. In Fig. 2(a) we show the effect of the evanescent modes on the Wigner delay time at energies just below where the second channel opens and, as we expect, there is a considerable increase in the delay of the electron. The absolute value of the amplitude c_1 of the first evanescent mode also increases just before the second propagating channel opens as shown in Fig. 2(b). The effect of the first evanescent mode c_1 is dominant since the amplitudes of the second and higher evanescent modes are near zero. A similar behavior of the evanescent modes occurs at energies just below where the third propagating channel opens. There again, one evanescent mode becomes dominant. In Figs. 2(c) and Fig. 2(d) we compare the behavior of first and second partial Wigner delay times τ_1 and τ_2, respectively, both for the case when the contributions of the evanescent modes are included and for the case when they are removed in calculations of the S matrix in this energy regime.

We have looked at the effect of evanescent modes on S-matrix elements in the two mode energy regime by computing the differences, $|S_{11}^0| - |S_{11}|$ and $|S_{12}^0| - |S_{12}|$, where S_{11}^0 and S_{12}^0 denote elements of the S matrix without contributions from evanescent modes. The difference in the magnitude of the S-matrix elements is small (of order 10^{-3}), but the difference in the slopes can be fairly large.

We have also looked at the analytic continuation of S-matrix elements in the complex energy plane and we find good agreement with the predictions of Wigner delay time plots. In Fig. 3, we show partial Wigner delay times in energy interval, $4E_1 < E < 9E_1$. In Fig. 4 we show the behavior of $|S_{11}|$ in the complex energy plane. Figure 4(a) gives large scale behavior, and Fig. 4(b) focuses on behavior near the real axis. The poles near to real energy axis [shown in Fig. 4(b)] determine the sharp peaks in the Wigner delay times. The poles further from the real axis determine the broader peaks in the Wigner delay time plots.

In Figs. 5 and 6 we show the effect of the energy dependence of the coupling matrices, $\bar{w}_{Np}$ and $\bar{w}_{Ne}$. This energy dependence is always neglected in RRMT calculations
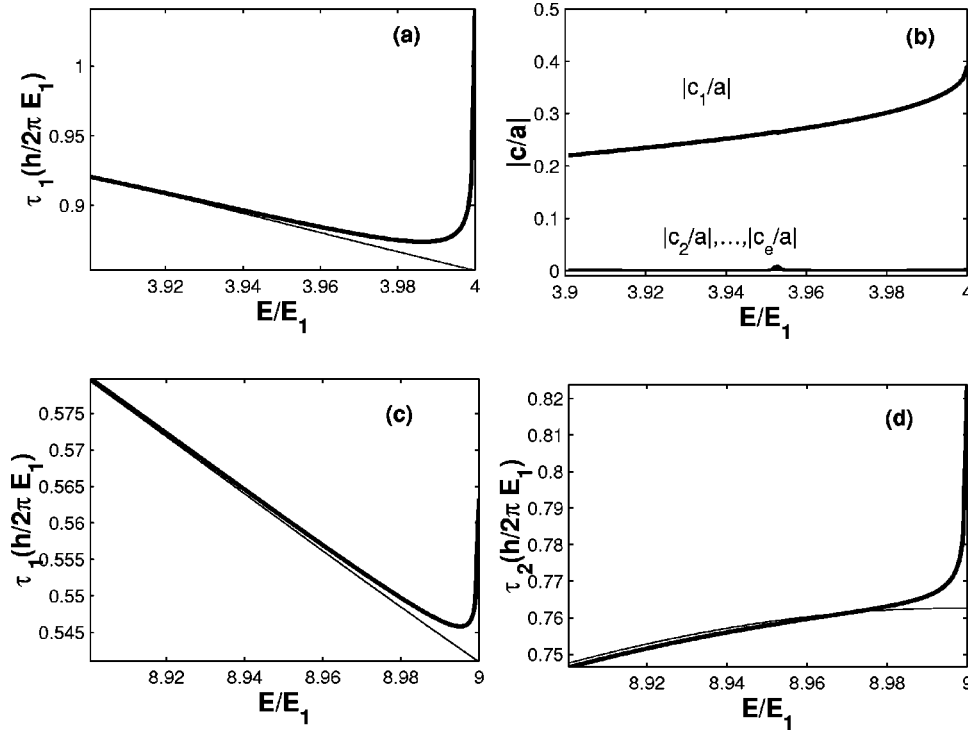
FIG. 2. Effect of evanescent modes for a waveguide with parameters $a = 10$ Å, $d = 100$ Å, $L = 500$ Å. (a) The solid line is Wigner delay time τ_1 in the one channel regime for an energy interval just before a second propagating channel opens in the lead. The dashed line shows τ_1 when no evanescent modes are included in calculations. (b) The amplitudes c_1 and c_2 of the first two evanescent modes in the same energy interval as in (a). (c) The solid line shows the first partial Wigner delay time, τ_1 just before the opening of the third channel. The dashed line is for the case when no evanescent modes are included in calculating τ_1. (d) The same as (c) for the second partial Wigner delay time, τ_2.

(RRMT calculations also neglect $\bar{w}_{Ne}$). In Fig. 5, we plot $|S_{11}|$, both for the case when the energy dependence of $\bar{w}_{Np}$ and $\bar{w}_{Ne}$ is taken into account (full line), and for the case when the energy dependence of $\bar{w}_{Np}$ and $\bar{w}_{Ne}$ is fixed at the value, $E = 6.5E_1$ (dotted-dashed line). In Fig. 6, the effect of the energy dependence of $\bar{w}_{Np}$ and $\bar{w}_{Ne}$ on the distributions of poles in the complex energy plane is shown. The position of S-matrix poles changes when the variation with energy of the coupling constants, $\bar{w}_{Np}$ and $\bar{w}_{Ne}$, is not included. In Fig. 6, the solid lines are contour lines of $|S_{11}|$ for the reaction

matrix calculation with the energy dependence of $\bar{w}_{Np}$ and $\bar{w}_{Ne}$ included. The dashed lines show the same quantity but using coupling matrices, $\bar{w}_{Np}$ and $\bar{w}_{Ne}$, with dependence on energy E fixed at the real value $E = 6.5E_1$. We also included eigenvalues of the effective Hamiltonian, $\bar{H}_{eff} = \bar{H}_{in} + \bar{w}_{Ne}\bar{w}_{eN}^\dagger - i\bar{w}_{Np}\bar{w}_{pN}^\dagger$, as cross marks on this plot. The eigenvalues of $\bar{H}_{eff}$ are calculated fixing the energy dependence of $\bar{w}_{Ne}$ and $\bar{w}_{Np}$ at the value $E = 6.5E_1$. The matrix, $\bar{H}_{eff}$ has the same number of eigenvalues as the number of cavity basis states used (2500) in the calculation of the reac-
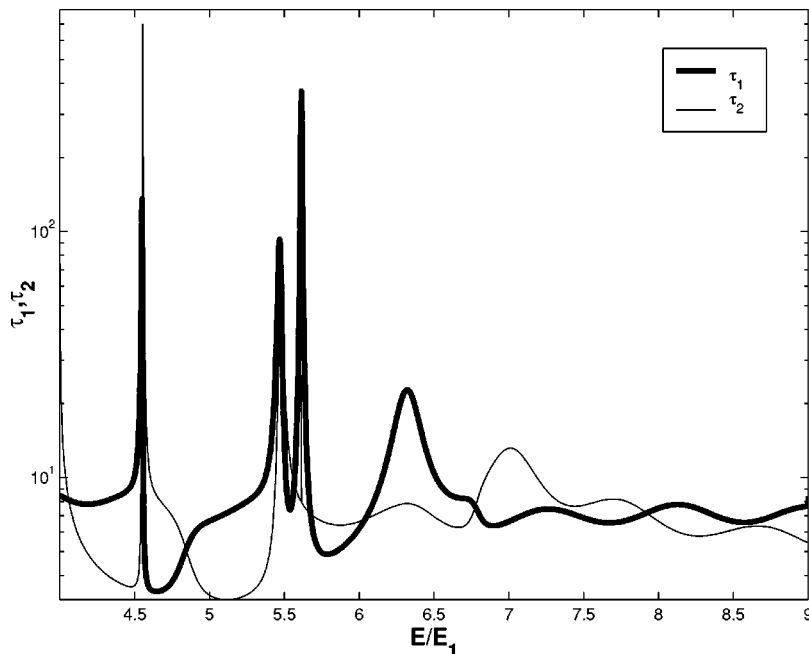
FIG. 3. Wigner delay times for the energy region when there are two modes in leads. The waveguide parameters are $a = 10$ Å, $d = 100$ Å, $L = 500$ Å.
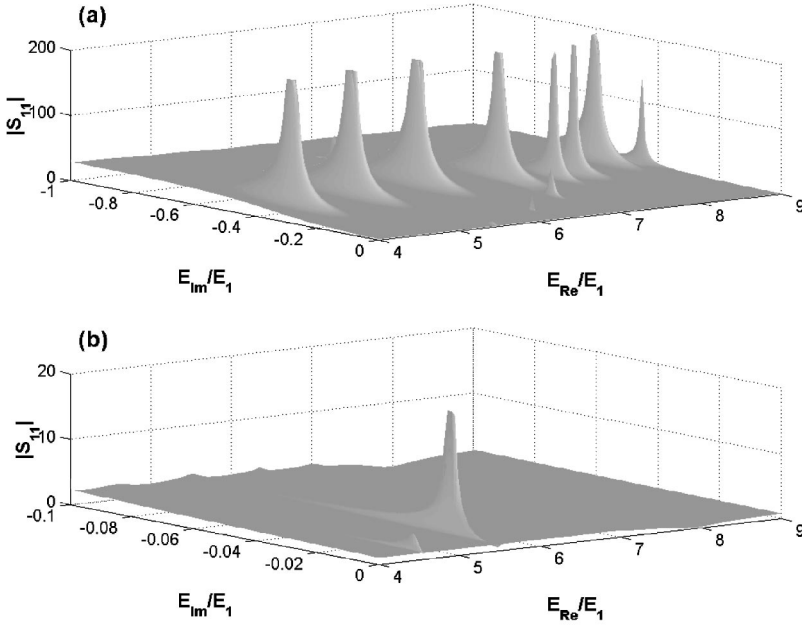
FIG. 4. Poles of the S matrix in lower complex energy plane when there are two modes in lead. The waveguide parameters are $a = 10$ Å, $d = 100$ Å, and $L = 500$ Å. The absolute value of first $\bar{S}$ matrix element S_{11} is shown. (a) S_{11} for imaginary energies in interval $0 \leqslant \mathrm{Im}(E) \leqslant -0.95$. (Only points for which $|S_{11}| < 200$ are shown.) (b) Same as in (a) but S_{11} is shown with imaginary energies very close to real axis, $0 \leqslant \mathrm{Im}(E) \leqslant -0.07$.

tion matrix. In Figure 6, we indicate with crosses, those eigenvalues of $\bar{H}_{eff}$ that are located in the energy interval $4E_1 < E < 9E_1$. Neglect of the energy dependence of the coupling constants causes a shift of the poles away from their true positions. This shift is small in the neighborhood of the fixed energy $E = 6.5E_1$, but it grows as one moves further away in energy.

VII. THE SIGNATURES OF CHAOS

In this section we compute the statistical properties of the Wigner delay times [23] obtained for deterministic scattering of the electron from the ripple cavity. The reaction matrix theory is especially suited for this type of computation. With the help of the coordinate transformation method in Sec. V,

we are able to compute a large number of basis states accurately by solving a single eigenvalue problem. We can then use these basis states to compute the scattering matrix for any energy, E. In contrast to this, when one uses finite element methods, or other mesh based numerical methods, to compute the S matrix, one must solve a large (but sparse) matrix equation for each energy E. Also, the reaction matrix approach can deal with any cavity size, but the mesh based methods cannot. For the purpose of computing Wigner delay times for chaotic cavities, we will change slightly the shape of rippled wall to have an amplitude, $y = d + a \sin(5\pi x/L)$, rather than $y = d + a \cos(4\pi x/L)$ as was used in preceding sections. This will allow the electrons to enter the cavity, rather than being reflected at the entrance when $a > d/2$.

We will compute the statistical distribution of Wigner de-
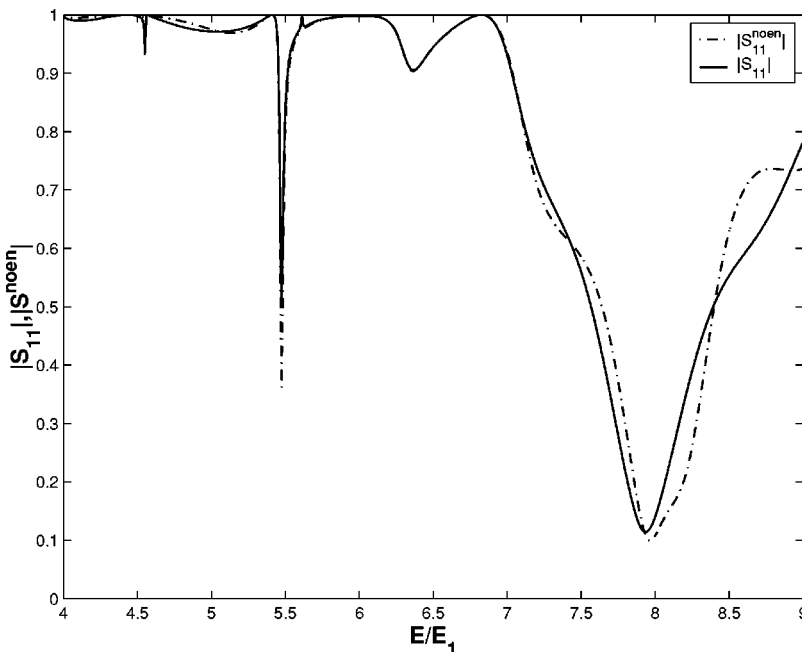
FIG. 5. Comparison of the first matrix element S_{11} when we take into account the energy dependence of the coupling matrices $\bar{w}_{Np}$ and $\bar{w}_{Ne}$ (solid line) to the first matrix element S_{11}^{noen} when the energy dependence of $\bar{w}_{Np}$ and $\bar{w}_{Ne}$ has a fixed value $E = 6.5E_1$ (dotted-dashed line). The cavity parameters the waveguide parameters are $a = 10$ Å, $d = 100$ Å, and $L = 500$ Å.
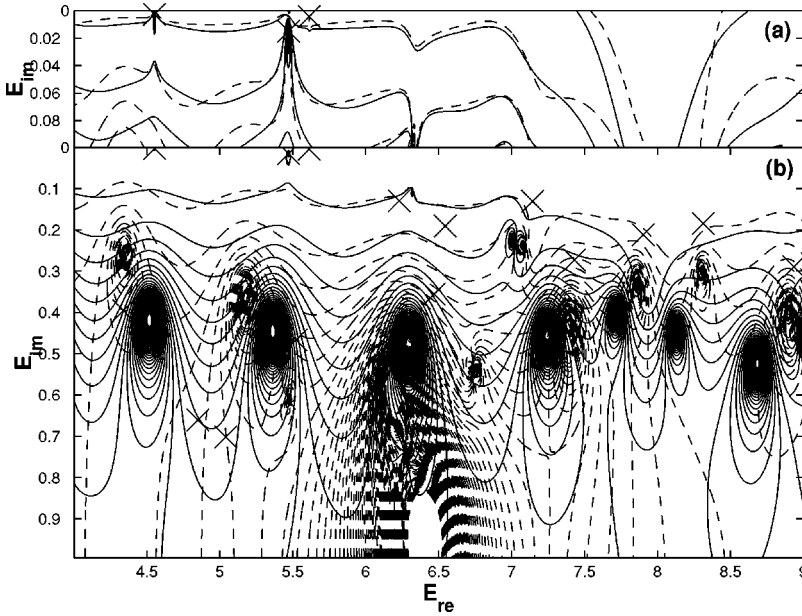
FIG. 6. Change of absolute value of $|S_{11}|$ when we take into account the energy dependence of the coupling matrices $\bar{w}_{Np}$ and $\bar{w}_{Ne}$ (solid line) and when of the energy dependence of $\bar{w}_{Np}$ and $\bar{w}_{Ne}$ has a fixed value $E=6.5E_1$ (dashed line). The crosses represent the eigenvalues of effective Hamiltonian, $\bar{H}_{eff}=\bar{H}_{in}-\bar{w}_{Ne}\bar{w}^{\dagger}_{eN}+i\bar{w}_{Np}\bar{w}^{\dagger}_{pN}$ in this energy region with energy fixed at $E=6.5E_1$. The cavity parameters $a=10$ Å, $d=100$ Å, $L=500$ Å. (a) Expanded view near real axis. (b) Poles further down the imaginary axis. (Only points for which $|S_{11}|$ <200 are shown.)

lay times, both for the case when the classical dynamics of the cavity is fully chaotic [24–26], and for the case where it has a mixed phase space. In Fig. 7, we plot Poincare surfaces of section (PSS) for several different values of ripple amplitude a. The surfaces of section are plots of Birkoff coordinates (p_x,x), of a classical particle each time it bounces off the section of the cavity at $y=0$. x is the position of the particle and p_x is its component of momentum parallel to the wall, each time it strikes the wall. Figure 7(a) shows the PSS for $a=1$, Fig. 7(b) is for the case $a=5$, and Fig. 7(c) is for the case $a=10$. The classical dynamics has a mixed phase space for small values of a. However, for $a\geq60$ it is almost fully chaotic, as shown in Figure 7(d).

One can use either Eq. (26) or Eq. (29) to calculate Wigner delay times for the case of deterministic scattering. We have checked that they give identical answers. For the case of deterministic scattering, we looked at two different parameter ranges to see how the statistical distribution of Wigner delay times changes as the underlying dynamics undergoes a transition from a mixed phase space to a fully chaotic phase space. For the regime with mixed phase space, we collected data by computing the Wigner delay times for 20 different values of ripple amplitude a ranging from $a=0.5$ Å to $a=10$ Å in units of 0.5 Å. In Figs. 8(a)–(c), we show histograms of the total Wigner delay times for deterministic scattering with a mixed classical phase space in the cavity, for cases when $M=2$, $M=6$, and $M=16$ propagating modes, respectively, exist in the leads. In these figures, $P(\tau)$ is the histogram of Wigner delay times normalized so the area is equal to 1, and $\langle\tau\rangle$ is the mean Wigner delay time. Each histogram contains 3 200 000 Wigner delay times. We see that the distributions are narrowly peaked around their average values. There is a shift toward more centralized (Gaussian-like) distribution when we increase number of
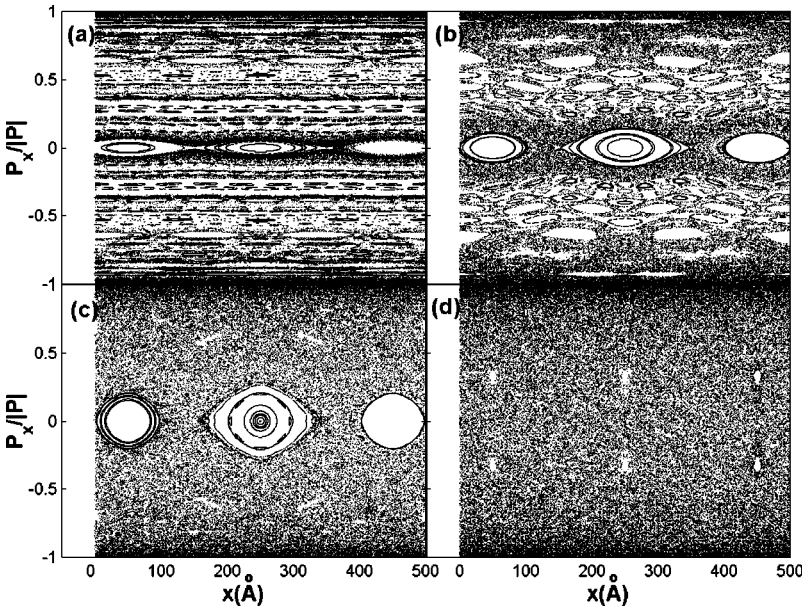
FIG. 7. PSS for the Birkhoff coordinates along the wall, $y=0$, of a classical particle in a closed billiard with the shape of the cavity. x is the position where the particle hits the wall and and p_x is its component of momentum parallel to the wall. (a) $a=1$ Å, $d=100$ Å, $L=500$ Å; (b) $a=5$ Å, $d=100$ Å, $L=500$ Å; (c) $a=10$ Å, $d=100$ Å, $L=500$ Å; and (d) $a=60$ Å, $d=100$ Å, $L=500$ Å.
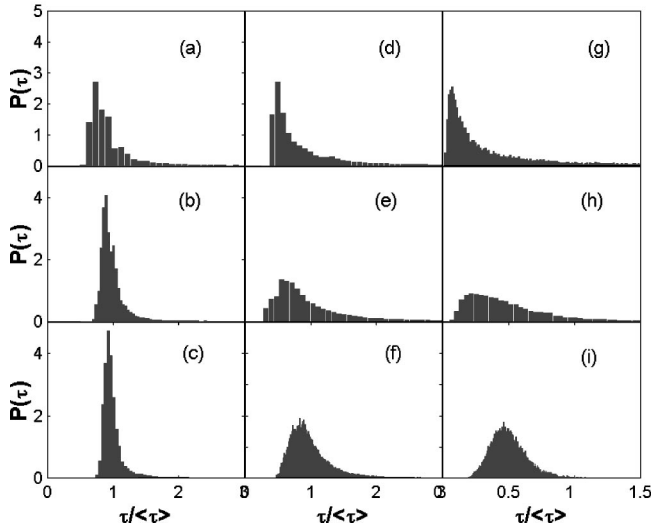
FIG. 8. Histograms of Wigner delay times for different numbers of propagating channels, M for the case of deterministic scattering [(a)–(c)] in the near integrable regime, [(d)–(f)] deterministic scattering in the chaotic regime; and (g)–(i) RRMT predictions. (a) Deterministic scattering in near integrable regime with $M=2$ for $0.5 \leqslant a \leqslant 10.0$ in steps of $a=0.5$ and with $d=100$ Å, $L=500$ Å; (b) same as (a) for $M=6$; (c) same as (a) for $M=16$; (d) $M=2$ in fully chaotic regime with $M=2$ for $60 \leqslant a \leqslant 75$ in steps of $a=1.0$ and with $d=100$ Å, $L=500$ Å; (e) same as (d) for $M=6$; (f) same as (d) for $M=16$; (g) RRMT result for $M=2$; (h) same as (g) for $M=6$; and (i) same as (g) for $M=16$.

channels. However, for the case of mixed phase space the system has a smaller number of resonances and the resonances are more sharply peaked than for the fully chaotic regime, and therefore the Wigner delay times are narrowly distributed.

For the regime with fully chaotic phase space we collected data for 15 different values of ripple amplitude, ranging from $a=60$ Å to $a=75$ Å in units of 1 Å. In Figs. 8(d)–(f), we show histograms of the total Wigner delay times for deterministic scattering with a fully chaotic classical phase space in the cavity, for cases when $M=2$, $M=6$, and $M=16$ propagating modes, respectively, exist in the leads. Each histogram contains 800 000 Wigner delay times. The distribution $P(\tau)$ shifts from a Poisson-like distribution to Gaussian-like distribution as we increase the number of channels. For a small number of channels the distribution is asymmetric and has a long tail.

We also looked at the statistics of the total Wigner delay times obtained by replacing the S matrix in Eq. (29), by the equation

$$\bar{S} = -\left(1 + 2i\bar{w}^{\dagger} \frac{1}{E\bar{1}_N - \bar{H}_{GOE} - i\bar{w}\bar{w}^{\dagger}} \bar{w}\right), \quad (38)$$

where $\bar{H}_{GOE}$ is chosen from an Gaussian orthogonal ensemble (GOE) and the coupling matrix $\bar{w}$ is constructed from the M eigenvectors of one realization of the $M \times M$ Hamiltonian matrix $\bar{H}_{GOE}$ in the GOE ensemble. We also checked

our result by building $\bar{w}$ using the M eigenvectors of each realization of $\bar{H}_{GOE}$, and we get a similar distribution for the corresponding number of channels. In Figs. 8(g)–(i), we show histograms of the total Wigner delay times obtain using $\bar{H}_{GOE}$ and its eigenvectors to construct the S matrix, for the cases $M=2$, $M=6$, and $M=16$, respectively. We see that the Wigner delay time statistics, for deterministic scattering, approaches the random matrix predictions as the degree of underlying chaos increases.

It is useful to note that we have calculated the Wigner delay times by taking the derivative of the S-matrix eigenphase curve, $\theta(E)$ vs E, in two different ways. The first way is to take two neighboring energy points (we chose $E=0$ and $E=0.001$) and use these to obtain one Wigner delay time for each realization of H_{GOE}. The second way is to obtain a whole series of Wigner delay times from the $\theta(E)$ vs E curve for a single realization of H_{in}. We have checked that these two methods give similar results.

The distribution of total Wigner delay times for our deterministic scattering from the chaotic ripple cavity, agrees qualitatively with the predictions of the random matrix theory. This agreement can be understand looking at the distribution of nearest neighbor energy eigenvalue spacings for $\bar{H}_{in}$. We have checked this distribution and have found it to be in good agreement with the distribution of nearest neighbor eigenvalues spacings obtained for H_{GOE}. Both satisfy the Wigner distribution [27]. Also the coupling constant $\bar{w}_{Np}$ that we obtained from the deterministic calculation is somewhat in similar form to that obtained from the GOE Hamiltonian. In Fig. 9(a), we show the coupling vector, $\bar{w}_{1p}\bar{K}_P^{-1}$, obtained from the GOE Hamiltonian. In Figs. 9(b) and 9(c), respectively, we show the coupling vectors, $\bar{w}_{1p}\bar{K}_P^{-1}$ as is defined in Eq. (27), for a nearly integrable system (with $a=5$ Å), and a fully chaotic system (with $a=70$ Å). The coupling vector $\bar{w}_{1p}$ for the deterministic system, becomes more random as we go to a fully chaotic regime.

VIII. CONCLUSION

In this paper we have studied the effect that evanescent modes have on the scattering properties of an electron in a waveguide with a ''chaotic'' cavity. We have reformulated the reaction matrix theory of electron waveguide scattering to explicitly include the effect of evanescent modes. We have found that evanescent modes can increase the delay of the electron for energies near the opening of new channels. This effect has been seen before [28]. The scattering system we have considered is relatively ''soft.'' There are no impurities and no sharp corners to snag evanescent modes, and yet their effect is still noticeable. For systems with impurities and sharp corners, we expect the effect of evanescent modes to be even more dramatic.

We have also studied the effect of neglecting the energy dependence of the coupling matrices that appear in the reaction matrix approach to scattering. This appears to cause an effective repulsion on the positions of quasibound state poles.
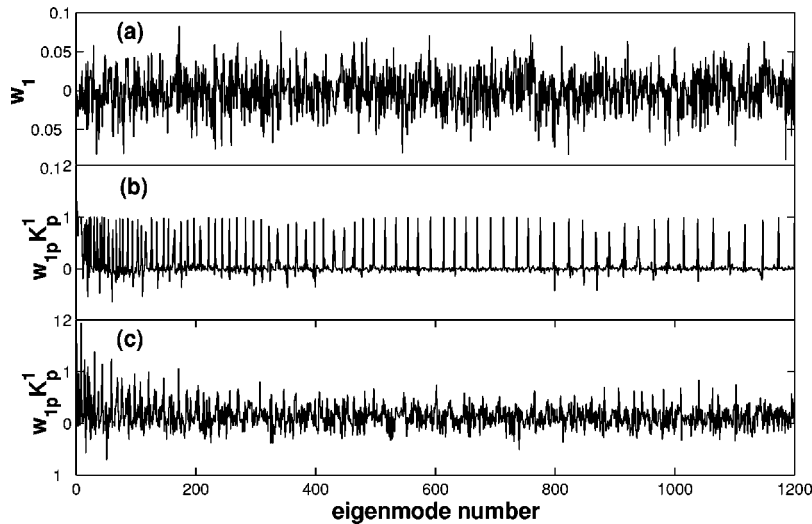
FIG. 9. Coupling matrix, $\bar{w}_{1p}$ (a) obtained from GOE; (b) for mixed phase space $a = 5$ Å; and (c) for chaotic phase space, $a = 60$ Å.

The effects of both the evanescent modes and the energy dependence of coupling matrices are routinely neglected in RRMT, and this should be kept in mind when attempting to use that theory to make predictions about real waveguide scattering experiments or numerical simulation of deterministic waveguide scattering systems.

We have also studied the statistical distribution of the Wigner delay times for scattering from our chaotic waveguide cavity, for the case of $M = 2$, $M = 6$, and $M = 16$ propagating modes. To build adequate statistics for comparison with RRMT predictions, we have included data for a range of ripple amplitudes, being careful to include data only from the regime where the internal dynamics of the ripple cavity is either mixed or completely chaotic. We find fairly good qualitative agreement with the predictions of RRMT for the case when the deterministic scattering occurs from a cavity that is classically chaotic.

[1] E.P. Wigner, Oak Ridge National Laboratory Report No. ORNL-2309 (unpublished).

[2] S.W. McDonald and A.N. Kaufman, Phys. Rev. Lett. **42**, 1189 (1979).

[3] R. Blumel and U. Smilansky, Phys. Rev. Lett. **64**, 241 (1990).

[4] Eyal Doron and U. Smilansky, Nonlinearity **5**, 1055 (1991).

[5] H.U. Baranger, R.A. Jalabert, and A.D. Stone, Chaos **3**, 665 (1993).

[6] W.A. Lin, J.B. Delos, and R.V. Jensen, Chaos **3**, 655 (1993).

[7] Pierre Gaspard and Stuart A. Rice, J. Chem. Phys. **90**, 2225 (1989).

[8] C. Rouivenez and U. Smilansky, J. Phys. A **28**, 77 (1995).

[9] Gursoy B. Akguc and L.E. Reichl, J. Stat. Phys. **98**, 813 (2000).

[10] E.P. Wigner and L.E. Eisenbud, Phys. Rev. **72**, 29 (1949).

[11] A.M. Lane and R.G. Thomas, Rev. Mod. Phys. **30**, 257 (1958).

[12] C. Bloch, Nucl. Phys. **4**, 503 (1957).

[13] H. Feshbach, Ann. Phys. (N.Y.) **19**, 287 (1962).

[14] Charles E. Porter and Norbert Rosenzweig, Physica A **44**, (1960); see also Charles E. Porter, *Statistical Theories of Spectra: Fluctuations* (Academic Press, New York, 1960).

[15] C.M. Marcus, R.M. Westervelt, P.f. Hopkins, and A.C. Gossard, Chaos **3**, 643 (1993).

[16] H.-J. Stockmann and J. Stein, Phys. Rev. Lett. **64**, 2215 (1990).

[17] E. Wigner, Phys. Rev. **73**, 1002 (1948).

[18] W. Meyerhof, Phys. Rev. **129**, 692 (1963).

[19] F. Barker and P. Treacy, Nucl. Phys. **38**, 33 (1962).

[20] D. Inglis, Nucl. Phys. **30**, 1 (1962).

[21] L.E. Reichl and Gursoy Akguc, Found. Phys. **31**, 2 (2001).

[22] G.A. Luna-Acosta, Kyungsan Na, L.E. Reichl, and A. Krokhin, Phys. Rev. E **53**, 3271 (1996).

[23] D. Bohm, *Quantum Theory* (Prentice-Hall, Englewood Cliffs, N.J., 1950), p. 260; E.P. Wigner, Phys. Rev. **98**, 145 (1955); F.T. Smith, *ibid.* **118**, 349 (1960).

[24] C.H. Lewenkopf and H.A. Weidenmuller, Ann. Phys. (N.Y.) **212**, 53 (1991).

[25] Y.V. Fyodorov and H-J. Sommers, J. Math. Phys. **38**, 1918 (1997).

[26] S. Albeverio, F. Haake, P. Kurasov, M. Kus, and P. Seba, J. Math. Phys. **37**, 4888 (1996).

[27] L.E. Reichl, *The Transition to Chaos in Classical Conservative Systems: Quantum Manifestations* (Springer-Verlag, New York, 1992).

[28] Daniel Boese, Markus Lischka, and L.E. Reichl, Phys. Rev. B **61**, 5632 (2000).